

# Weather Observation by an Electronically Scanned Dual-Polarization Phase-Tilt Radar

Krzysztof A. Orzel and Stephen J. Frasier<sup>ID</sup>

**Abstract**—A dual-polarized X-band solid-state 1-D electronic scanning “phase-tilt” weather radar (PTWR) and its scanning geometry are presented. In this architecture, the true elevation angle decreases from the nominal array tilt angle and the true azimuth angle increases from the requested azimuth as one scans off boresight. Additionally, this scanning geometry induces a canting angle effect, which can be significant especially at higher elevation tilts. The predictions of potential biases in selected polarimetric variables due to this effect are derived. For elevation angles below 10°, where polarimetric measurements are of most value, predicted biases are negligible. The PTWR was deployed in Arlington, TX, USA, for an eight-week period during Spring 2014 collecting data on a number of weather events. The direct proximity (250 m away) of a mechanically scanning magnetron-based radar, employing a dual-polarized parabolic antenna allowed for a qualitative and quantitative data comparison. We find the differences in the observations made by the two radar systems are not attributable to the aforementioned biases, but appear primarily due to differences in sampling volumes of the two radars. We also find that at high-elevation tilts, the coupling of the true elevation angle with the array-relative azimuth scan angle complicates the interpretation of features at a constant altitude such as the melting layer.

**Index Terms**—Meteorological radar, phased arrays, radar polarimetry.

## I. INTRODUCTION

THE advent of phased-array technology for meteorological applications has been realized recently with the development of research platforms such as the National Weather Radar Testbed [1], [2], mobile Doppler radars for rapid scanning [3]–[5], and low-cost low-power polarimetric phased arrays [6]–[8]. These and related emerging technologies are summarized in [9]. With these and initiatives such as the Multimission Phased-Array Radar, the subsequent Spectrum Efficient National Surveillance Radar (SENSR), and the Center for Collaborative Adaptive Sensing of the Atmosphere (CASA), there is a growing interest in the potential for use of phased-array radars in weather surveillance and measurement. However, because the operational weather radar networks of the United States and several other countries

Manuscript received May 4, 2017; revised October 21, 2017 and December 5, 2017; accepted December 6, 2017. This work was supported by the National Science Foundation through the University of Massachusetts Amherst under Grant AGS-1318148. (Corresponding author: Stephen J. Frasier.)

The authors are with the Microwave Remote Sensing Laboratory, Department of Electrical and Computer Engineering, University of Massachusetts, Amherst, MA 01003 USA (e-mail: frasier@ecs.umass.edu).

Color versions of one or more of the figures in this paper are available online at <http://ieeexplore.ieee.org>.

Digital Object Identifier 10.1109/TGRS.2017.2782480

are now adopting dual polarization, it is anticipated that it will be necessary for future phased-array systems to support polarimetry for improved hydrometeor identification and rainfall estimation, with the same fidelity (or nearly so) as is possible with today’s reflector antennas.

Zhang *et al.* [10], Zrnic *et al.* [11], and others have described the polarization biases evident in phased-array scans. These arise from the fact that, unlike reflector antennas, which realize only a single boresight beam, phased arrays scan their beam over a wide range of angles relative to the boresight of the elements that comprise the array. It is this scanning away from the boresight direction of the radiating elements that gives rise to changes in the polarization of the radar. That is, once scanned off the principal planes of the antenna, the radiated fields deviate from purely horizontal and vertical. The deviation from these desired polarizations gives rise to measurement biases that are theoretically correctable.

The Microwave Remote Sensing Laboratory at the University of Massachusetts has developed an X-band dual-polarization phase-tilt weather radar (PTWR) capable of electronic scanning in the azimuth dimension while mechanically tilting in elevation [12]. During Spring 2014, the PTWR was deployed for a period of eight weeks atop a building on the University of Texas campus in Arlington, TX, USA. The deployment site was located within the Dallas-Fort Worth Urban Demonstration Network operated by the CASA Engineering Research Center [13]–[15]. The proximity of a CASA X-band radar offered the opportunity for comparison of a solid-state phased-array observations and magnetron-based mechanically scanned systems. Both systems were nearly collocated, which allowed for a quantitative comparison of products from the two radar systems.

In this paper, we briefly describe the PTWR’s characteristics, expected performance compared with mechanically scanned systems, and report the results of the Spring 2014 experiment. The following section describes the two radars used in the study and the anticipated biases. The next section describes the experimental setting and observations. Discussion and conclusions follow.

## II. RADAR DESCRIPTION

A photograph of the PTWR is shown in Fig. 1, and a system-level block diagram is shown in Fig. 2. The PTWR system consists of an array antenna, an array controller, an up/downconverter, an intermediate frequency (IF) digital transceiver, a host computer, and a pedestal. The antenna subsystem is a 1-D dual-polarization active array antenna



Fig. 1. PTWR deployed on the roof of Nedderman Hall at the University of Texas-Arlington. Inset: PTWR in the laboratory with radome and one panel of radiating elements removed to reveal the TR modules.

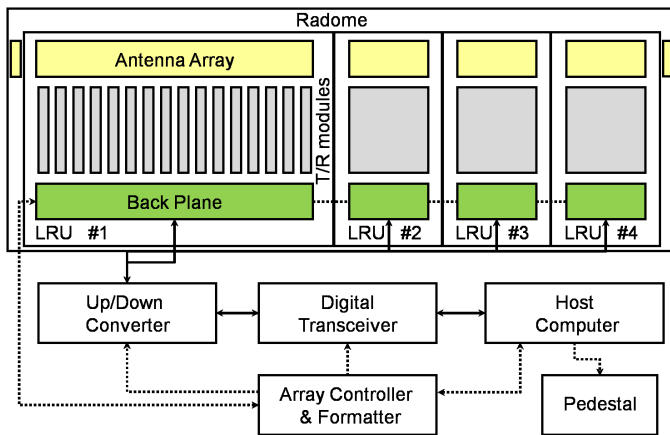


Fig. 2. PTWR system block diagram indicating control (dotted lines) and signal flow (solid lines).

that enables electronic scanning in the azimuth plane, while scanning in the elevation plane is performed mechanically. This type of antenna architecture reduces the number of required T/R modules and hence significantly decreases the overall system cost. The antenna subsystem is designed with a modular approach employing four identical “line replaceable units” (LRUs) to facilitate quick replacement or future system extensions. An array controller provides configuration and timing signals for all subsystems (with the exception of the pedestal). Owing to the low peak power provided by the solid-state transmit/receive (TR) modules, implementation of pulse compression techniques is required for the radar to achieve satisfactory sensitivity. A nonlinear frequency-modulated waveform is produced by an arbitrary waveform generator within the digital IF transceiver (Pentek 7140), which is upconverted and transmitted by the array. Upon reception of radar echoes, the signal is downconverted and is sampled in its uncompressed form. A signal processing thread in the host computer implements pulse compression and computes weather radar dual-polarization products [16], [17].

The host computer generates all scanning settings, executes the signal processing, and controls the data flow. The following sections provide further details on the individual subsystems.

### A. Antenna Array

The full antenna assembly is a planar structure of 72 columns of microstrip patches. Each column is a single element of the linear array and is itself a dual-linear polarized subarray composed of 32 aperture-coupled patches interconnected by a series feed network for each polarization. Here, two serpentine feed lines excite each radiating element in both polarizations. Although a series feed, when compared with its corporate alternative, exhibits lower transmission loss and requires less substrate area, its performance is frequency dependent, which limits the antenna bandwidth. The central 64 columns of the antenna array are fed by dedicated TR modules while the remaining eight outer columns (four at each end) are terminated passive elements so as to reduce the effects of diffraction and nonuniform mutual coupling at the edges of the array [18]. The 64 active elements of the array are arranged in four LRUs with each LRU consisting of 16 antenna elements, 16 corresponding TR modules, and a dc power and signal distribution backplane.

The phase-tilt antenna allows scanning of  $\pm 45^\circ$  in the horizontal plane with a beamwidth of  $1.8^\circ$  in azimuth at broadside and  $3.5^\circ$  in elevation. Fig. 3 shows the co-polar (HH) and cross-polar (VH) array-averaged element pattern and a sample co-polar and cross-polar beam pattern for a beam directed  $3^\circ$  from broadside. These patterns were measured by a near-field scanner. Directivity is 36.9 dB for the co-polar beam. The cross-polar pattern exhibits a null at boresight, though with somewhat high shoulders in the elevation plane that contribute considerably to the two-way integrated cross-polar ratio (ICPR2). The ICPR2 is defined as

$$\text{ICPR2} = \frac{\int f_c(\theta, \phi) f_x(\theta, \phi) \sin \theta d\theta d\phi}{\int f_c^2(\theta, \phi) \sin \theta d\theta d\phi} \quad (1)$$

where  $f_c$  and  $f_x$  are the respective co-polar and cross-polar normalized radiation patterns. The measured ICPR2 is  $-17.8$  dB. We note that this is slightly worse than the  $-20$  dB value that is recommended by Wang and Chandrasekar [19] and others. An ICPR2 of  $-20$  dB or better guarantees that bias in differential reflectivity,  $Z_{dr}$ , is limited to under 0.2 dB for any possible value of differential phase.

### B. T/R Modules

Behind each antenna element is a TR module. A block diagram of a TR module is presented in Fig. 4. Each TR module consists of a control block, a diversity switch, and transmit and receive channels. The operation of each TR module is controlled by an onboard field-programmable gate array (FPGA) that is accessed and configured by the array controller. A custom-designed high-power four-port diversity switch is a star configuration of four GaAs single-pole single-throw p-i-n diode switches. It is characterized by an insertion loss less than 3 dB and isolation in excess of 45 dB over the frequency band 9–9.6 GHz. The transmitter block consists of a

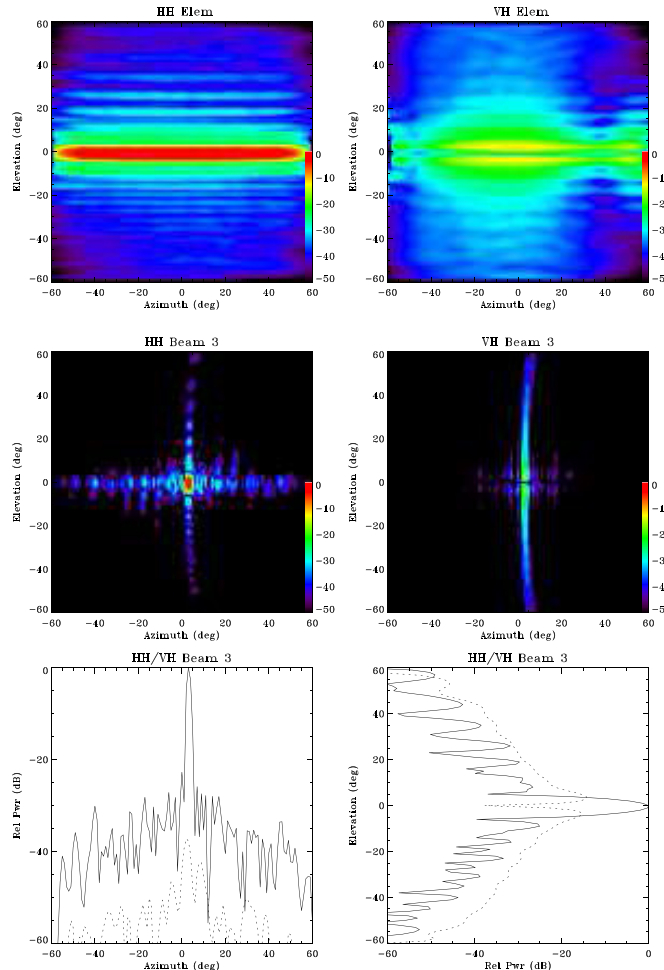


Fig. 3. (Top) Averaged co- and cross-polarized element radiation patterns, (Middle) sample co- and cross-polarized beam patterns, and (Bottom) principal plane cuts of the beam patterns obtained from near-field antenna range measurements. Solid lines denote co-polarized and dotted lines denote cross-polarized patterns. Measured patterns extend to  $\pm 60^\circ$ , though scanning in azimuth is limited to  $\pm 45^\circ$

medium- and a high-power amplifier yielding a transmit peak power of about 1.25 W at the antenna ports. The receiver block consists of a low-noise amplifier and a gain block. A common-leg architecture is used, in which the phase shifter, gain block, and variable attenuator are shared between the transmit and receive channels [20]. This configuration features  $360^\circ$  of phase control with  $5.6^\circ$  of resolution and 31.5 dB of amplitude control with 0.5 dB of resolution. The common part of the circuit is connected to the independent input and output ports by means of two switches. To distribute RF signals to the TR modules, two 64-way power divider/combiner networks are used to divide (combine) the radar waveform upon transmission (reception). The LRUs are interconnected via a backplane. The backplane provides dc power distribution and a 25-MHz low-voltage differential signal bus for fast programming and communication to the TR modules.

#### C. Array Controller

A core component of the PTWR is the array controller that is implemented in an FPGA. The array controller loads lookup

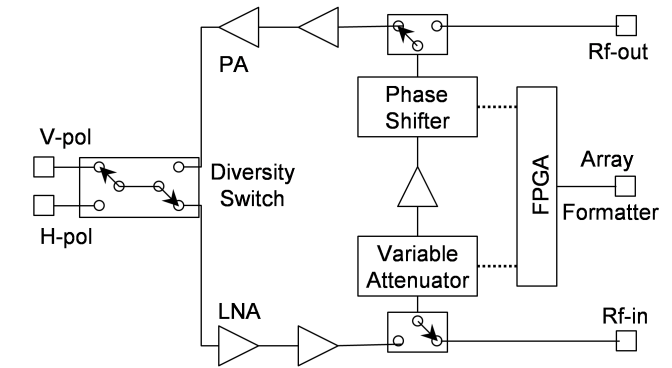


Fig. 4. TR module block diagram. Antenna ports are on the left. Rf-out is the transmit port, and Rf-in is the receive port.

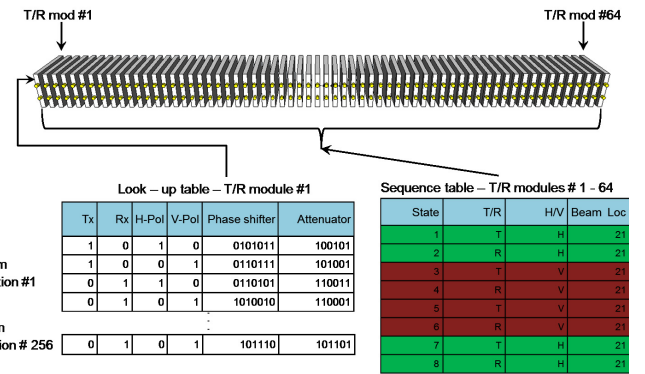


Fig. 5. (Left) Beam location LUT contains digital words for individual TR module mode, attenuation, and phase settings. (Right) The ST selects beams and is common to all TR modules.

tables (LUTs) and sequence tables (STs) for all TR modules. The LUT (Fig. 5) contains precalculated settings for the phase shifter and digital attenuator of each TR module to switch to the requested beam location. The LUT defines 256 beam positions in four modes of operation (TR for H/V polarization). The structure of the LUT is common for all TR modules, but the settings for the phase shifter and attenuator are specific to the individual TR module depending on its location in the array. On system power-up, the array controller uploads the LUTs to the individual TR modules.

The radar operator then specifies the requested beam locations and polarimetric mode of operation. This information forms the beam ST (Fig. 5), which defines units of four pulses. Sequences are repeated if desired to collect more pulses per beam. Since the ST holds only memory register addresses, which are common for all TR modules, the array controller broadcasts a single ST simultaneously to all TR modules. The timing information (pulse length and pulse repetition time individually defined for pulses 1–4) is then passed from the host computer to the array controller that executes a state machine driving the control signals for the array and the transceiver. This procedure is repeated for each beam.

#### D. Transceiver

The antenna is driven by a conventional single-channel superheterodyne pulse-compression radar transceiver.

The transmit waveform is produced at an IF of 60 MHz by a digital-to-analog converter, and a dual-stage upconverter translates it to the RF transmit frequency centered at 9.36 GHz. A high-power solid-state amplifier boosts the signal power prior to 64-way division for the individual TR modules. A portion of this signal is coupled directly back to the receiver, so the transmitted waveform may be sampled for use in the subsequent pulse compression. Upon reception, the 64-way combined signal is downconverted to IF and sampled by the digital receiver.

This phased-array design permits calculation of all polarimetric products, but because only a single channel is available for transmission or reception, it also requires the alternate transmit/alternate receive (ATAR) mode of operation. Thus, four pulses (HH, HV, VH, and VV) are required to obtain all combinations of polarizations contained in the scattering matrix.

### III. POLARIZATION PROPERTIES

While phased arrays offer advantages such as inertia-less and arbitrary scanning and improved clutter suppression via fixed dwells, they also present challenges for weather radar applications. These include variation in gain and beamwidth with scan angle, as well as variations in polarization properties.

The effects of phased-array scanning on polarization have been described by Zhang *et al.* [10] and Zrnic *et al.* [11] who modeled the dual-polarized radiating elements as crossed dipoles. Lei *et al.* [21] considered waveguide apertures and microstrip patches as radiating elements. These studies have shown that the polarization basis becomes nonorthogonal when the array scans in a direction away from the principle planes of the radiating elements. In addition, owing to the difference in element radiation patterns, the difference in the radiation pattern amplitude alone can produce a significant error in the measured product if left uncorrected. For example, a horizontal electric dipole produces a horizontal electric field that varies as the cosine of the azimuth angle, whereas a vertical electric dipole produces a vertical electric field that is independent of azimuth angle.

Prior studies have derived biases in polarimetric products for scan angles relative to the array face. When relating to world coordinates, it is assumed the array is oriented vertically such that the broadside direction is horizontal. In practice, the array face is also tilted so as to allow scanning in elevation both above and below the array boresight. For the phase-tilt antenna, which can scan only in the horizontal principle plane, the antenna must be physically tilted to scan in elevation. The combination of mechanical tilt followed by azimuth scanning in the now-tilted plane yields a rotation of polarization basis by an angle  $\gamma$  relative to true horizontal and vertical polarizations. This is depicted in Fig. 6(a).

Another consequence of the azimuthal scanning from a tilted array face is the coupling of true elevation angle and azimuth scan angle. As one scans off boresight, the true elevation angle decreases from the nominal array tilt angle and the true azimuth increases from the requested azimuth. The dependence of the true elevation and azimuth angles and

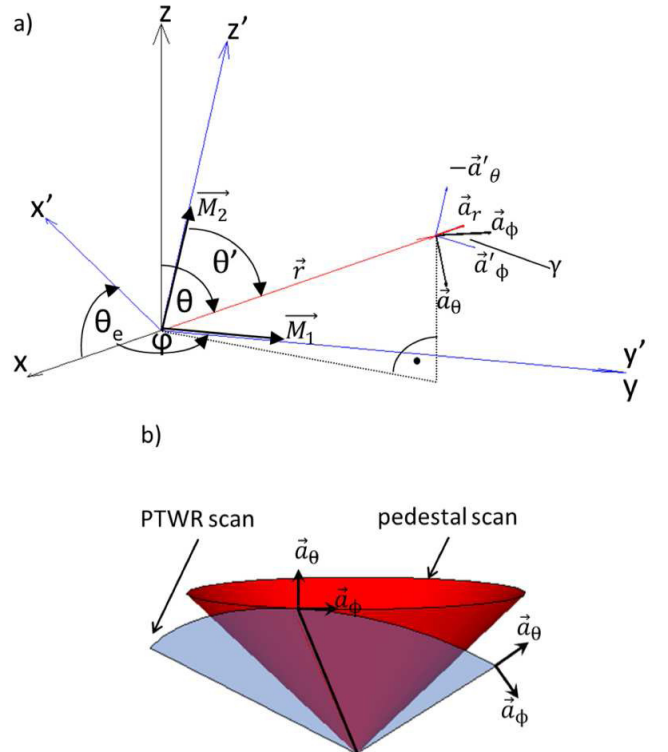


Fig. 6. (a) Spherical coordinate system for electric fields radiating from a pair of dipoles having moments  $\vec{M}_1$  and  $\vec{M}_2$ . Unit vectors  $\vec{a}_\phi$ ,  $\vec{a}_\theta$ ,  $\vec{a}'_\phi$ , and  $\vec{a}'_\theta$  lie in the same plane perpendicular to  $\vec{r}$ . Array-relative H and V polarizations remain orthogonal across the scan, but they rotate as one scan away from broadside. (b) Azimuthal scan from a tilted array face scans one face of a pyramid rather than the cone described by mechanical scanning.

the polarization rotation on electronic scan angle is derived in the Appendix. The result of the polarization basis rotation is potential bias in measured radar products. Below are summarized the results for several polarimetric products.

#### A. Reflectivity Factor and Differential Reflectivity

The horizontal and vertical reflectivity factors  $Z'_{h,v}$  measured under no polarization rotation condition are defined as

$$Z'_{h,v} = \frac{4\lambda N}{\pi |K_w|^2} \langle |s'_{hh,vv}|^2 \rangle \quad (2)$$

where  $N$  is the number density of scatterers per unit volume,  $\lambda$  is the wavelength,  $K_w$  is a term involving the complex refractive index of the scatterers, and  $s'_{hh,vv}$  are the co-polar (diagonal) terms of the received backscattering matrix. The definition of  $Z'_{h,v}$  includes propagation effects as described in the Appendix. Using the development described there, the horizontal and vertical polarization reflectivity factors and the differential reflectivity measured by a phase-tilt radar can be expressed as

$$\begin{aligned} Z_h^{(p)} &= \frac{4\lambda N}{\pi |K_w|^2} \langle |s_{hh}^{(p)}|^2 \rangle \\ &= \cos^4(\gamma) Z'_h + \sin^4(\gamma) Z'_v + \frac{1}{2} \sqrt{Z'_h Z'_v} \operatorname{Re}[\rho'_{hv}] \sin^2(2\gamma) \end{aligned} \quad (3)$$

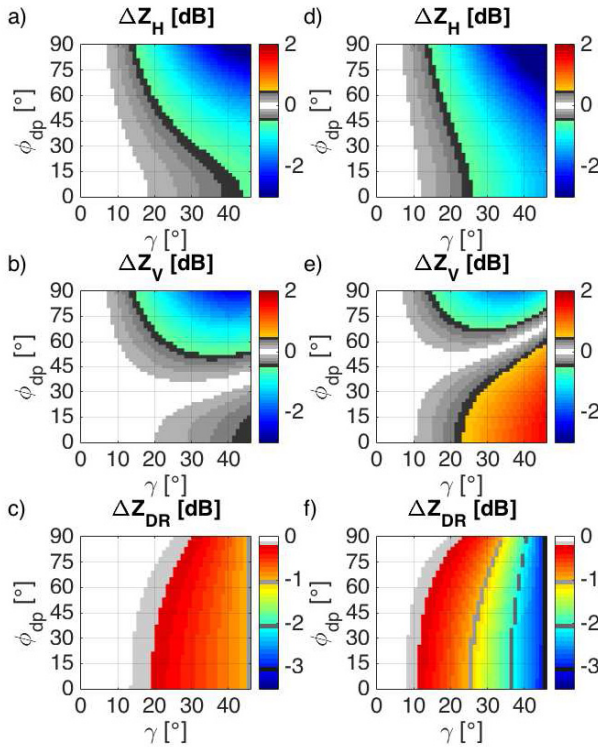


Fig. 7. Dependence of reflectivity and differential reflectivity bias on the polarization rotation angle  $\gamma$ . Parameters used in the simulation are (a)–(c)  $Z_{DR} = 1$  dB, (d)–(f)  $Z_{DR} = 3$  dB, and  $\rho_{hv} = 0.98$  in all cases. White indicates the region where bias is less than 0.1 dB.

$$\begin{aligned} Z_v^{(p)} &= \frac{4\lambda N}{\pi |K_w|^2} \langle |s_{vv}^{(p)}|^2 \rangle \\ &= \sin^4(\gamma) Z'_h + \cos^4(\gamma) Z'_v + \frac{1}{2} \sqrt{Z'_h Z'_v} \operatorname{Re}[\rho'_{hv}] \sin^2(2\gamma) \end{aligned} \quad (4)$$

$$\begin{aligned} Z_{DR}^{(p)} &= \langle |s_{hh}^{(p)}|^2 \rangle / \langle |s_{vv}^{(p)}|^2 \rangle \\ &= \frac{\cos^4(\gamma) Z'_{dr} + \sin^4(\gamma) + \frac{1}{2} \sqrt{Z'_{dr}} \operatorname{Re}[\rho'_{hv}] \sin^2(2\gamma)}{\sin^4(\gamma) Z'_{dr} + \cos^4(\gamma) + \frac{1}{2} \sqrt{Z'_{dr}} \operatorname{Re}[\rho'_{hv}] \sin^2(2\gamma)} \end{aligned} \quad (5)$$

where the (p)-superscripts denote variables subject to polarization rotation, whereas the terms without superscripts denote intrinsic values in the absence of rotation. The retrieval biases for radar reflectivity and differential reflectivity expressed in decibels are defined as

$$\begin{aligned} \Delta Z_{h,v} &= 10 \log_{10} \left( \frac{Z_{h,v}^{(p)}}{Z'_{h,v}} \right) \\ \Delta Z_{DR} &= 10 \log_{10} \left( \frac{Z_{dr}^{(p)}}{Z'_{dr}} \right) \end{aligned} \quad (6)$$

where  $Z_{h,v}^{(p)}$ ,  $Z'_{h,v}$ ,  $Z_{dr}^{(p)}$ , and  $Z'_{dr}$  are in linear units.

Equations (3)–(5) reveal that  $Z_h^{(p)}$ ,  $Z_v^{(p)}$ , and  $Z_{DR}^{(p)}$  depend on  $Z'_h$  and  $Z'_v$  as well as the co-polar correlation coefficient,  $\rho'_{hv}$ , and the effective canting angle,  $\gamma$ . Fig. 7 shows the reflectivity and differential reflectivity bias, for the ATAR mode, as a function of the polarization rotation angle,  $\gamma$ . Parameters used in the calculation are:  $Z_{DR} = 1$  dB [Fig. 7(a)–(c)],  $Z_{DR} = 3$  dB [Fig. 7(d)–(f)], and  $\rho_{hv} = 0.98$ ,  $0^\circ \leq \gamma \leq 45^\circ$

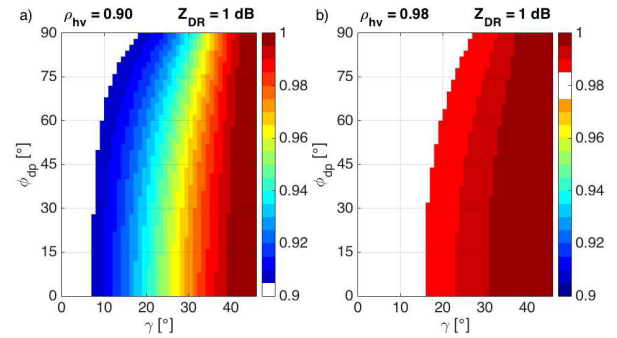


Fig. 8.  $\rho_{hv}^{(p)}$  of a phase-tilt radar for (a) hail (b) rain.  $Z_{DR} = 1$  dB in all cases.



Fig. 9. Map of the Dallas-Fort Worth radar network during the spring 2014 deployment. The PTWR was installed in direct proximity to the CASA XUTA X-band radar on the campus of University of Texas-Arlington. The Fort Worth WSR-88D radar (KFWS) was located 25 km to the southwest and the C-band TDWR radar (TDFW) was located 40 km to the northeast. XMML and XFTW are two other CASA radars not used for this comparison.

in all cases. The biases are more pronounced with increasing  $Z_{DR}$  and rotation angle  $\gamma$ . It can be seen that the horizontal reflectivity factor is biased low whereas the bias in vertical reflectivity can be either positive or negative, depending on the value of differential propagation phase  $\phi_{dp}$ . The differential reflectivity is biased low. This parameter is related to the oblateness of the hydrometeors. Note that for  $\gamma = 45^\circ$ , the return from both polarizations is expected to be the same, and hence  $Z_{DR}^{(p)} = 0$  dB. This is clearly visible in Fig. 7(c) where  $\Delta Z_{DR}(\gamma = 45^\circ) = -1$  dB and Fig. 7(f) where  $\Delta Z_{DR}(\gamma = 45^\circ) = -3$  dB. Finally, it is evident that if  $\gamma \leq 10^\circ$ , the bias in  $\Delta Z_{DR} \leq 0.1$  dB. This corresponds to the radar field of view where the tilt angle  $\Theta_e < 10^\circ$  (see Fig. 15), which is where quantitative measurements of precipitation are desired.

### B. Correlation Coefficient

The measured co-polar correlation coefficient  $\rho'_{hv}$  under no polarization rotation condition is defined as

$$\rho'_{hv} = \frac{\langle s_{hh}'^* s_{vv}' \rangle}{\sqrt{\langle |s_{hh}'|^2 \rangle \langle |s_{vv}'|^2 \rangle}} = \rho_{hv} \exp(j\phi_{dp}). \quad (7)$$

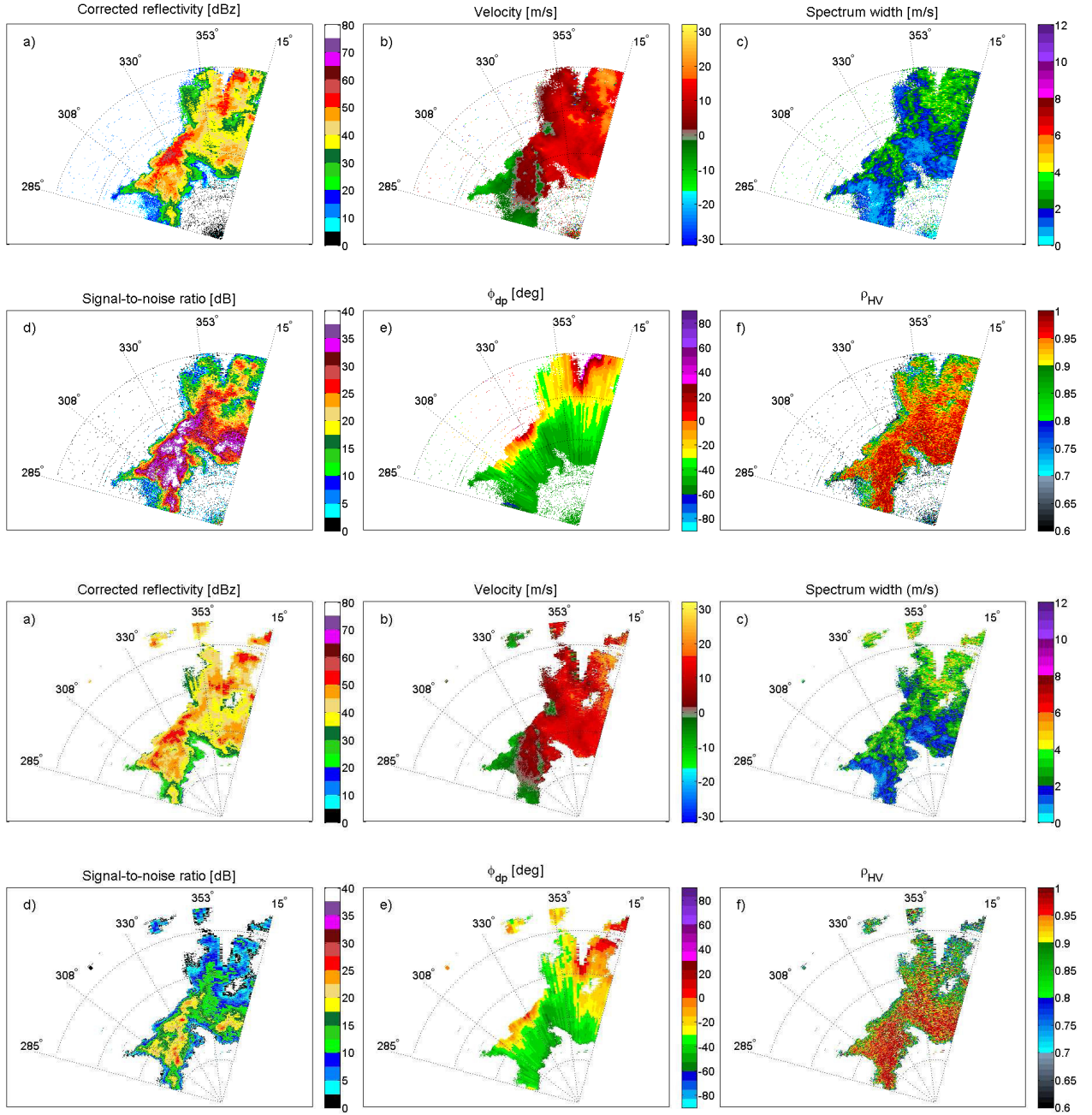


Fig. 10. Squall line observations on April 4, 2014. First and Second rows: radar products provided by CASA XUTA at 01:10:09 UTC at 5.3° elevation tilt. Products include (a) attenuation corrected reflectivity factor, (b) Doppler (radial) velocity, (c) Doppler spectrum width, (d) signal-to-noise ratio, (e) differential phase, and (f) co-polar correlation coefficient. Third and fourth rows: corresponding radar products provided by PTWR at 01:10:07 UTC at 6° elevation tilt. Range rings are spaced 10 km apart.

Using the definitions given in (7) and (23), the correlation coefficient measured by a phase-tilt radar is

$$\rho_{hv}^{(p)} = \frac{\langle s_{hh}^{(p)*} s_{vv}^{(p)} \rangle}{\sqrt{\langle |s_{hh}^{(p)}|^2 \rangle \langle |s_{vv}^{(p)}|^2 \rangle}} = \frac{\rho'_{hv} \cos^4 \gamma + \rho'^{*}_{hv} \sin^4 \gamma + \frac{1}{4} (Z'_{dr}^{1/2} + Z'^{-1/2}_{dr}) \sin^2 2\gamma}{\sqrt{\cos^4 \gamma + Z'^{-1}_{dr} \sin^4 \gamma + \frac{1}{2} \operatorname{Re}[\rho'_{hv}] Z'^{-1/2}_{dr} \sin^2 2\gamma}} * \frac{1}{\sqrt{Z'_{dr} \sin^4 \gamma + \cos^4 \gamma + \frac{1}{2} \operatorname{Re}[\rho'_{hv}] Z'^{1/2}_{dr} \sin^2 2\gamma}}. \quad (8)$$

The correlation coefficient  $\rho_{hv}^{(p)}$  is biased high and depends on  $Z'_{dr}$ ,  $\rho_{hv}$ , and rotation angle  $\gamma$ . The dependence of  $\rho_{hv}^{(p)}$  on  $Z'_{dr}$  is negligible within the range of  $Z'_{dr}$  values expected for meteorological targets. The bias in  $\rho_{hv}^{(p)}$  is more significant for lower values of  $\rho_{hv}$  as shown in Fig. 8, which compares  $\rho_{hv}$  simulated for hail [Fig. 8(a)] and rain [Fig. 8(b)] cases. Based on a typical setting of hydrometeor-type classification boundaries [19], [22] defined that the correct classification of rain, hail, and bright band observations requires bias in the correlation coefficient to be less than 2%, 5%, and 10%, respectively. This condition is satisfied in all cases as long as  $\gamma \leq 20^\circ$ .

TABLE I  
RADAR SYSTEM SPECIFICATIONS

Parameter	PTWR	XUTA	TDWR	WSR-88D
Peak power [kW]	0.06	11	250	500
Frequency [GHz]	9.36	9.41	5.6	3
Polarization	dual	dual	single	dual
ATAR	STSR	STSR	STSR	
Az beam width [°]	1.8-2.6	1.8	0.5	1.25
El beam width [°]	3.6	1.8	0.5	1.25
$\Delta R$ [m]	60	60	150	1000
Max range [km]	45	40	460	460
PRF [kHz]	2-3	1.6-2.4	0.8-1.1	0.3-1.3
Azimuth Sector [°]	90	360	360	360
Pulse width [ $\mu$ s]	20	0.6	1.1	1.57-4

#### IV. OBSERVATIONS

During April to June 2014, the PTWR was installed on the roof of Nedderman Hall on the campus of the University of Texas-Arlington as shown in Fig. 1. At the same time, the CASA UT-Arlington Radar, designated XUTA, was located nearby atop Carlisle Hall located to the south and slightly east. Obstructions on the Nedderman Hall rooftop blocked the line of sight between the radars and views toward the east, but afforded comparable views to the southwest and to the northwest by the PTWR. Initial tests revealed no evidence of radio frequency interference by either radar system.

The CASA XUTA radar is an X-band dual-polarization radar that is part of the Dallas-Fort Worth Urban Demonstration Network. It employs a 1.2-m-diameter parabolic dish antenna mounted on an elevation-over-azimuth scanning pedestal [23]. It transmits both polarizations simultaneously and employs a dual-channel receiver; thus, the polarization scheme is simultaneous transmit/simultaneous receive (STSR). Whereas the PTWR employs solid-state transmitters and pulse compression, the XUTA employs an 11-kW magnetron source that is divided equally between polarizations upon transmission. Although the average powers of the two systems are similar, the higher gain antenna of the CASA radar lends it greater sensitivity.

Fig. 9 shows all of the weather radars operating in proximity to the PTWR and XUTA radars. These include the Fort Worth Weather Surveillance Radar (WSR), 1988, Doppler (WSR-88D—KFWs), the Terminal Doppler Weather Radar (TDFW) at DFW airport, and two additional X-band CASA radars, at Midlothian (XMDL) and Fort Worth (XFTW). Although XMDL was operating, due to the beam blockage of PTWR to the southeast, it was not used for data comparison. XFTW was not yet operational at the time of the experiment. The main characteristics of each radar are summarized in Table I.

A number of weather events were observed during the Spring 2014 PTWR deployment. During these events, the PTWR made regular scans over a 90° azimuthal sector at elevations of 2°, 6°, 10°, 14°, 18°, and 22°. At the same time, the XUTA radar was controlled by CASA Meteorological Command and Control software [24] performing adaptive sector scans at elevation angles of 1°, 2°, 3°, 5.3°, and 7.4°.

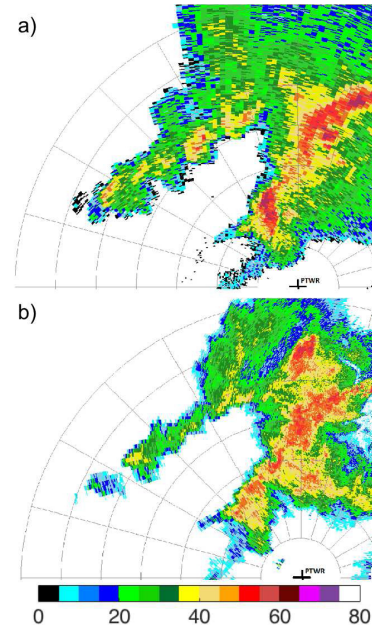


Fig. 11. Squall line observations on April 4 2014. Reflectivity provided by (a) WSR-88D radar (KFWs) at 01:11:21 UTC and (b) TDWR radar (TDFW) at 01:10:59 UTC at the lowest elevation tilts. The location of the PTWR is indicated with a black cross. Range rings are spaced 10 km apart. Finer angular and range spatial resolution provided by the TDWR radar is apparent.

For a qualitative comparison, Fig. 10 presents near-simultaneous dual-polarization products from the PTWR and XUTA radars obtained during the passage of a heavy precipitation event on April 4, 2014. Qualitatively, the observations are similar. In this case, the largest difference is in the sensitivities of the two X-band systems as indicated by the differing signal-to-noise ratios between XUTA and the PTWR. The approximately 15-dB difference is a consequence of the relatively short pulse length ( $20\mu$ s) in use at the time by the PTWR and by its lower antenna gain. The reflectivity images from both systems have been corrected for attenuation using schemes based upon the specific differential phase,  $K_{dp}$ .

For further reference, near-simultaneous scans of reflectivity collected by the S-band KFWs at 01:11:21 UTC and the C-band TDFW at 01:10:59 UTC on April 4, 2014 are shown in Fig. 11. These radars are not co-located and utilize different antennas. Hence, the shown reflectivity fields do not correspond to the same scattering volumes as do the X-bands. Nevertheless, the measured reflectivity fields are roughly comparable. Both radars detected heavy precipitation in excess of 50 dBz. The S- and C-band radars are less prone to attenuation than are the X-band radars.

Given the statistical uncertainty of individual measurements, biases due to polarization effects are too small to be obvious in instantaneous imagery. The statistical uncertainty of individual radar reflectivity measurements depends upon the number of independent samples (independent pulses) measured, which is target dependent. However, an uncertainty of approximately  $\pm 1$  dB is typical, representative of 15 independent pulses. Since the expected biases due to polarization effects are substantially less than this, we consider time-averaged measurements. To this end, the original radial data from both

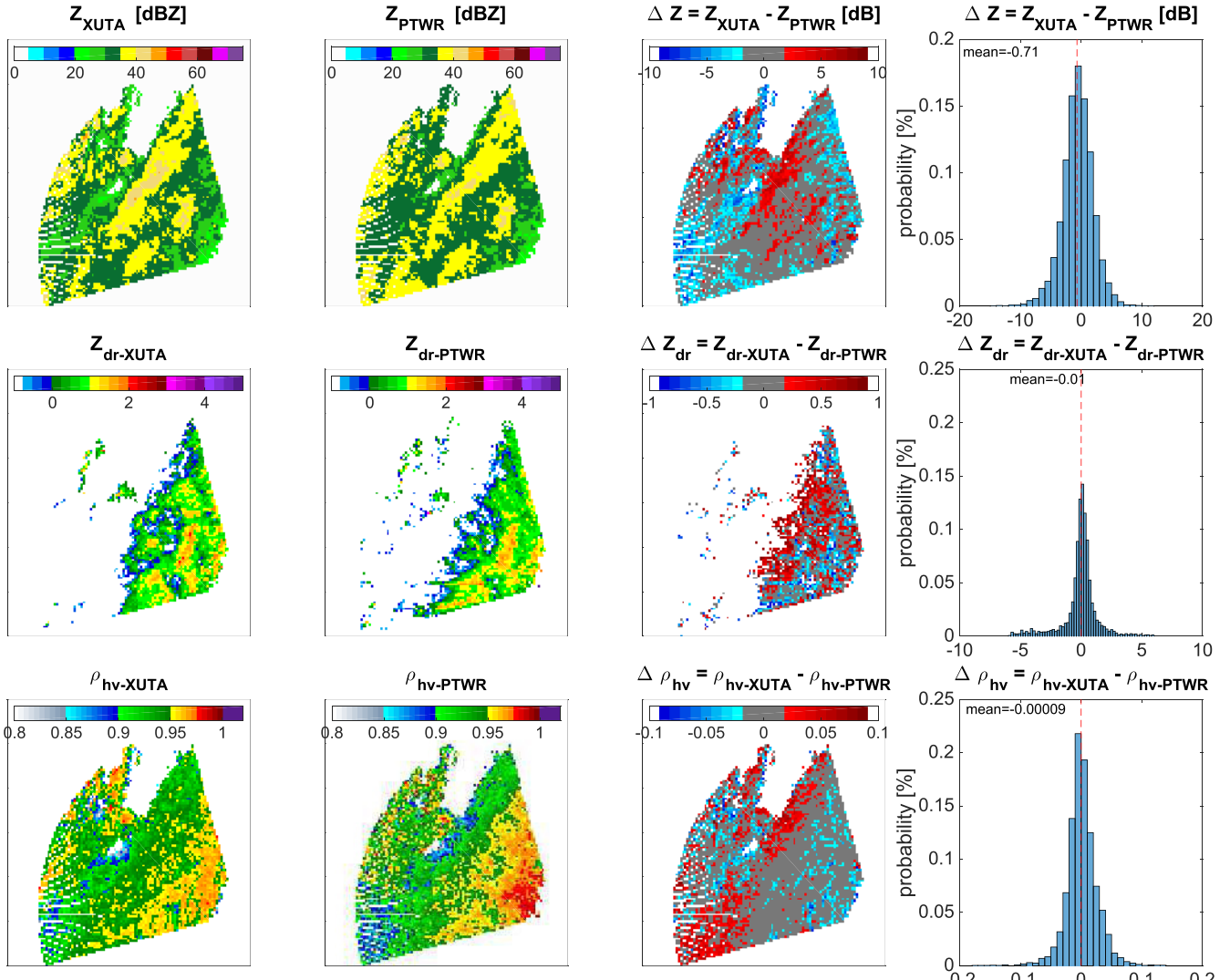


Fig. 12. Time-averaged PPIs of (attenuated) (Top) reflectivity factor  $Z$ , (Middle) differential reflectivity  $Z_{dr}$ , and (Bottom) co-polar correlation coefficient  $\rho_{hv}$  collected between 00:48 and 01:43 UTC on April 4, 2014 aligned to a common grid with a resolution of 500 m. From left to right: XUTA, PTWR, XUTA-PTWR difference, and histogram of pixel-wise difference.

radars up to 40 km range are aligned to a common grid with a resolution of 500 m. Each grid location represents the average of all data points associated with it for XUTA and PTWR, respectively. At least 20 radar resolution cells are averaged within each grid pixel. Multiple near-simultaneous scans by each radar collected over time are averaged in order to reduce statistical uncertainty. Only scans with a time difference less than 15 s between two radar systems are used, resulting in 24 scans over the observation period. Thus, the approximate number of independent samples contained in each gridded pixel is  $15 \cdot 20 \cdot 24 = 7200$ .

Fig. 12 shows comparisons of the time-averaged reflectivity factor  $Z$ , differential reflectivity  $Z_{dr}$ , and co-polar correlation coefficient  $\rho_{hv}$ . These show comparisons of the PTWR field of view with the nearby CASA XUTA radar obtained at elevations of  $6.0^\circ$  (PTWR) and  $5.3^\circ$  (XUTA). Compared are accumulated imagery collected between 00:48 and 01:43 UTC on April 4, 2014, during which a severe thunderstorm warning was issued. Data were thresholded on  $Z > 20$  dBZ,  $\rho_{hv} > 0.8$ , and SNR  $> 3$  dB. To avoid potential errors introduced

by differing attenuation corrections for each radar, we use attenuated variables in this comparison.

In these images, the polarization rotation angle scales with the azimuth angle relative to the center of the imaged sector, varying from  $0^\circ$  at the center to about  $4^\circ$  at the edges. Were the effects of polarization rotation on any of these products to be apparent, we would expect to see a variation with azimuth angle. Although root-mean-square differences of a few decibels are evident in the histogram of reflectivity difference, the time-average imagery and the difference image show no systematic differences between the reflectivity fields as a function of azimuth angle.

With perfect co-location of radar resolution volumes, the statistical uncertainty of the accumulated reflectivity differences would be given by  $\sigma_{\Delta Z} = 10 \log(1 + 2/\sqrt{7200}) \approx 0.1$  dB. From the histograms in Fig. 12, the observed scatter in the difference images is larger than this. It is believed the observed scatter in the measurements is largely a consequence of time differences and differing sampling volumes of the two radars (particularly in the elevation dimension). The largest

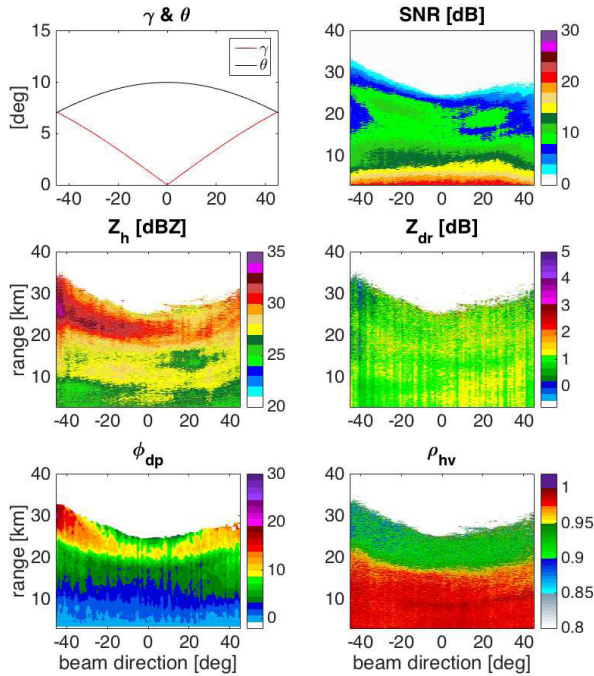


Fig. 13. Time-averaged PTWR radar products collected between 12:48 and 13:22 on June 9, 2014, at  $10^\circ$  nominal (broadside) elevation. The top-left panel shows the absolute value of canting angle,  $\gamma$  (red curve), and beam elevation (black curve) versus azimuth angle.

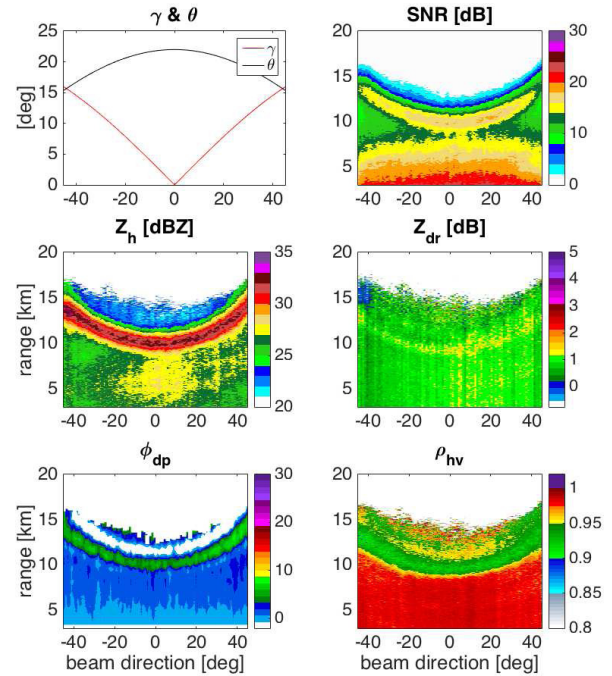


Fig. 14. As in Fig. 13 at  $22^\circ$  nominal (broadside) elevation.

positive  $\Delta Z$  ( $Z_{\text{XUTA}} > Z_{\text{PTWR}}$ ) appears in regions of highest reflectivity, and the lowest values ( $Z_{\text{XUTA}} < Z_{\text{PTWR}}$ ) appear in regions of lower reflectivity. These differences would be consistent with effects of the larger sampling volume of the PTWR (nonuniform beam filling) and/or to finite range sidelobes in the PTWR pulse compression. Differential reflectivity shows a slight positive difference between the two radars, but again little dependence upon azimuth. Finally, differences in co-polar correlation coefficient also appear largely independent of azimuth, but more dependent on range owing to the differing signal-to-noise ratios.

At the elevation angles for which direct comparison with the CASA radar was performed, it is not possible to attribute observed differences to the effective canting angle. Rather, differences in sampling volume appear to be more significant. In Figs. 13 and 14, we evaluate time-averaged PTWR echoes at substantially higher elevation angles. Here, observations of moderate rainfall over a period of 34 min on June 9, 2014, are considered.

Fig. 13 shows time-averaged imagery of radar products at  $10^\circ$  nominal elevation angle. Each panel represents an average of 24 scans. Images are shown in azimuth-versus-range format to better show features with scan angle at all ranges. The curved feature at 20-km nominal range is a bright-band echo associated with the melting layer at approximately 3.8-km altitude. It appears at more distant ranges at the scan edges because the true beam elevation at the scan edge is lower, approximately  $7^\circ$ . Thus, the bright band at a constant altitude appears curved in this image (it would appear as a straight-line feature orthogonal to the broadside direction in

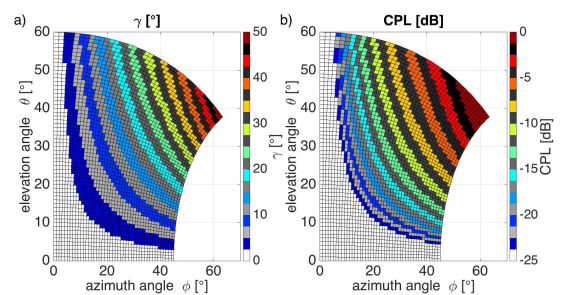


Fig. 15. (a) Polarization rotation angle  $\gamma$ . (b) Apparent CPL for elevation tilts  $\theta_e = [0, 60]$  and radar defined azimuth angle  $\phi' = [0, 45]$ .

a PPI-sector format). The bright-band echo corresponds to a notable drop in  $\rho_{hv}$ , a slight reduction in  $Z_{dr}$ , and abrupt increase in  $\phi_{dp}$  including the possible influence of backscatter differential phase. The polarization rotation varies from zero at broadside to about  $7^\circ$  at the edge of scan.

Fig. 14 shows time-averaged imagery of radar products at  $22^\circ$  nominal elevation. Here the true elevation at the edge of scan is approximately  $15^\circ$ , and the polarization rotation again varies from zero at broadside to approximately  $16^\circ$ . We observe a slight increase in  $Z_h$  and in  $Z_v$  (not shown) near the scan edge within and below the bright band,  $Z_{dr}$  remains essentially constant below the bright band, and  $\phi_{dp}$  is notably lower than that observed in Fig. 13 as a consequence of the shorter propagation path and the higher elevation angle.

These time-averaged imagery show behaviors not anticipated based upon the predictions of Section III. In particular, the predictions were based on known or constant values of the various parameters and do not capture how these parameters may vary as a function of elevation angle. Based on the theory presented in Section III, we expected  $Z_h$  to decrease slightly

with increasing canting angle at the scan edges. Instead, we see a slight increase. It is hypothesized that this is a consequence of the coupling of elevation angle with scan and of the wider beamwidth at scan edge. Reflectivity increases rapidly in the melting layer, and due to larger beamwidth and lower tilt angle, beams at the edges of scan intercept the melting layer over a longer path. Hence, we observe increased  $Z_h$ . The two variations are confounded in this measurement. Additionally, higher radar sensitivity in the central part of the scan can be noted, which is directly related to the increase in the antenna gain near broadside, as well as the shorter propagation path. As in Fig. 13, the bright-band feature in Fig. 14 is observed neither at a constant range nor at a constant elevation angle. Thus, the coupling of azimuth and elevation in the PTWR scan can complicate interpretation of imagery.

## V. CONCLUSION

In this paper, a dual-polarized short-range 1-D phased-array X-band weather radar was described. Predictions of its polarimetric response to weather targets indicate a rotation of transmitted and received polarizations with azimuth scan angle at a given mechanical tilt. The rotation is equivalent to an effective canting angle of the hydrometeors. The bias in the radar products due to the polarization rotation,  $\gamma$ , depends on the type of the observed weather as well as the differential propagation phase  $\phi_{dp}$ . For the phase-tilt configuration in general, this bias is expected to be negligible in all weather conditions as long as  $\gamma < 10^\circ$ , which corresponds to the antenna tilt  $\Theta_e < 10^\circ$ .

Comparisons of PTWR radar measurements with a mechanically scanning radar employing a parabolic dish revealed differences more attributable to differences in sampling volume than canting angle effects. The coupling of elevation and azimuth can complicate interpretation of observations at a constant range particularly for high-elevation scans. We note this coupling of elevation and azimuth is peculiar to the PTWR architecture.

It is also worth noting that if the PTWR antenna was rotated by  $90^\circ$ , such that electronic scanning occurred in elevation with mechanical scanning in azimuth, both the polarization rotation and elevation angle coupling effects are eliminated. This is because in such a case, the azimuthal scan is a rotation about the  $z$ -axis, rather than a tilted  $z$ -axis. This scheme is more consistent with conventional mechanical scanning, though it does not afford beam agility in azimuth.

Finally, this paper considered only a 1-D electronic scanning phased-array antenna. Such an antenna is constrained to scan in one of the principal planes of the antenna aperture, where the radiated polarizations are known to be orthogonal. A fully electronic scanning phased array (in both azimuth and elevation) is not constrained to scan only in the principal planes of the aperture. Thus, electronic scans can be performed at constant elevation angle, though they will necessarily deviate from the antenna's principal planes. Such scanning induces other effects, namely, the nonorthogonality of radiated polarizations. The severity of these effects and their compensation are a subject of future research.

## APPENDIX

The dependence of the polarization orientation on scan angle is based on a mode of a pair of crossed dipoles located at the coordinate system origin as presented in Fig. 6(a). For consistency, we assume the same conditions and use the same terminology as in [10], which described polarization properties for 2-D phased-array architecture.

In Fig. 6(a), the  $yz$  plane is perpendicular to the ground, while the antenna aperture is in the  $y'-z'$  plane. The coordinate system  $X'Y'Z'$  is obtained by rotation about the  $y$ -axis by the elevation angle  $\theta_e$ . The  $x'$ -axis represents the boresight of the radar system at elevation angle  $\theta_e$ .  $\vec{M}_1$  is the magnetic current density of a horizontally polarized radiating element, and  $\vec{M}_2$  is the magnetic current density of a vertically polarized radiating element.

The following transformation relates the level and tilted coordinates in the Cartesian system:

$$\begin{aligned}\vec{a}'_x &= \vec{a}_x \cos \theta_e + \vec{a}_z \sin \theta_e \\ \vec{a}'_y &= \vec{a}_y \\ \vec{a}'_z &= -\vec{a}_x \sin \theta_e + \vec{a}_z \cos \theta_e.\end{aligned}\quad (9)$$

In the spherical coordinate system, unit vectors are defined as follows:

$$\begin{aligned}\vec{a}'_\phi &= -\vec{a}_x \cos \theta_e \sin \phi' + \vec{a}_y \cos \phi' - \vec{a}_z \sin \theta_e \sin \phi' \\ \vec{a}'_\theta &= \vec{a}_x \sin \theta_e - \vec{a}_z \cos \theta_e.\end{aligned}\quad (10)$$

And, given that for the PTWR  $\theta' = 90^\circ$ , unit vectors in terms of the tilted coordinate system are

$$\begin{aligned}\vec{a}'_\phi &= -\vec{a}'_x \sin \phi' + \vec{a}'_y \cos \phi' \\ \vec{a}'_\theta &= -\vec{a}'_z.\end{aligned}\quad (11)$$

Projections of  $\vec{a}'_\phi$  and  $\vec{a}'_\theta$  onto the horizontal ( $\vec{a}_\phi$ ) and vertical ( $-\vec{a}_\theta$ ) directions yield

$$\begin{aligned}\vec{a}_\phi \cdot \vec{a}'_\phi &= \cos \theta_e \sin \phi \sin \phi' + \cos \phi \cos \phi' = \cos \gamma \\ -\vec{a}_\theta \cdot \vec{a}'_\phi &= -\sin \gamma \\ \vec{a}_\phi \cdot \vec{a}'_\theta &= \sin \gamma \\ -\vec{a}_\theta \cdot \vec{a}'_\theta &= \cos \gamma\end{aligned}\quad (12)$$

where angle  $\gamma$  defines the rotation of the local "horizontal" unit vector out of the horizontal plane. Furthermore, one can define the electric field at distance  $\vec{r}$  away from  $\vec{M}_1$  and  $\vec{M}_2$  as

$$\begin{aligned}\vec{E}_1 &= E_{t1}[-\vec{a}_x \cos \theta_e \cos \phi' \sin \phi' + \vec{a}_y \cos^2 \phi' \\ &\quad - \vec{a}_z \sin \theta_e \cos \phi' \sin \phi'] \\ &= E_{t1} \cos \phi' \vec{a}'_\phi \\ \vec{E}_2 &= E_{t2}[-\vec{a}_x \sin \theta_e + \vec{a}_z \cos \theta_e] = -E_{t2} \vec{a}'_\theta \\ E_{t1,2} &= \frac{k^2 e^{-jkr}}{4\pi\epsilon r} M_{1,2}.\end{aligned}\quad (13)$$

The factor  $\cos \phi'$  in the definition of  $E_1$  indicates a reduction of intensity of the H-field as the beam is directed away from broadside, which is a direct consequence of the dipole's electric field pattern. This effect can be measured during initial array calibration and included in the radar calibration constant on a beam-by-beam basis. An inspection of the electric fields

$E_1$  and  $E_2$  shows that both  $H'$  and  $V'$  polarizations remain orthogonal across the scan, since they are oriented along unit vectors  $\vec{a}'_\theta$  and  $\vec{a}'_\phi$ . However, note that  $\vec{a}'_\phi$  expressed in terms of the level coordinate system reveals a vertical component ( $\vec{a}_z$ ), which is produced by a horizontal dipole  $\vec{M}_1$ . This is the source of bias in polarimetric products.

Finally, it is important to point out that the 1-D phased-array radar azimuthal scan traces out a single face of a pyramid. This is distinct from the case of a mechanically rotated dish antenna system, which traces a section of a cone. In the case of the PTWR, the true beam elevation,  $\theta$ , decreases from the nominal elevation,  $\theta_e$ , as the beam is directed away from broadside. Similarly, the true azimuth,  $\phi$ , increases from the requested azimuth  $\phi'$  as the beam is directed away from broadside. The effect is more evident at higher elevation angles. The radar-defined beam direction ( $\phi', \theta_e$ ) is related to beam direction in the level coordinate system ( $\phi, \theta$ ) as

$$\tan \phi = \tan \phi' \sec \theta_e \quad (14)$$

$$\cos \theta = \cos \phi' \sin \theta_e. \quad (15)$$

### Scattering and Rotation Matrix

It is generally assumed that in most meteorological observations of interest, water drops take the form of oblate spheroids with a zero-mean canting angle, that is, the angle between the incident electric field and the axis of symmetry of a water drop. In this case, the off-diagonal components of the backscattering matrix can be ignored. However, in the case of the PTWR, there is a constant nonzero canting angle due to the orientation error in the polarization plane. This is a rather unusual phenomena observed in radar data [25]. Canted hydrometeors cause depolarization of linearly polarized  $H$  and  $V$  waves, but the effect of depolarization on co-polar variables is negligible if the canting angle is on the order of a few degrees [26]. Furthermore, Zrnic *et al.* [27] showed that bias due to cross-polar and co-polar radiation coupling is of higher importance in the case of the STSR mode of operation. Wang and Chandrasekar [19] also investigated a case of antenna feed alignment error, concluding that in the alternate mode of operation, orientation error up to  $5^\circ$  can be tolerated if an error  $\Delta Z_{DR}$  of 0.2 dB can be accepted.

Although the PTWR operates in the ATAR mode, the self-induced canting angle due to polarization rotation can exceed  $5^\circ$  (see Fig. 15). For example, if the beam direction is set  $45^\circ$  away from broadside and the array aperture is tilted by  $10^\circ$ , then the canting angle is  $7.1^\circ$ , which is equivalent to an apparent antenna cross-polarization isolation level (CPL) of around  $-18$  dB. The CPL and the polarization rotation angle are related by [19]

$$\text{CPL} = 20 \log_{10}(\tan \gamma). \quad (16)$$

Under polarization rotation-free conditions, the intrinsic radar backscattering matrix  $S^{(b)}$  is defined as

$$S^{(b)} = \begin{bmatrix} s_{hh}^{(b)} & s_{hv}^{(b)} \\ s_{vh}^{(b)} & s_{vv}^{(b)} \end{bmatrix} \quad (17)$$

Due to the symmetry of hydrometeors, it is assumed that  $s_{hv}^{(b)} = s_{vh}^{(b)}$ .

The transmission matrix,  $T$ , takes into account the effect of phase shift and attenuation due to wave propagation in atmosphere containing hydrometeors. The cross coupling of the  $H$  and  $V$  fields is negligible, and therefore the transmission matrix is assumed diagonal. It is defined as [28]

$$T = \begin{bmatrix} T_{hh} & 0 \\ 0 & T_{vv} \end{bmatrix}. \quad (18)$$

If the forward and back propagation effect is included, the received backscattering matrix is modified to [11]

$$\begin{aligned} S' &= TS^b T = \begin{bmatrix} T_{hh}^2 s_{hh}^{(b)} & T_{hh} T_{vv} s_{hv}^{(b)} \\ T_{hh} T_{vv} s_{hv}^{(b)} & T_{vv}^2 s_{vv}^{(b)} \end{bmatrix} \\ &= \begin{bmatrix} s'_{hh} & s'_{hv} \\ s'_{hv} & s'_{vv} \end{bmatrix}. \end{aligned} \quad (19)$$

The effect of polarization rotation can be included by the introduction of a rotation matrix

$$P(\gamma) = \begin{bmatrix} p_{11} & p_{12} \\ p_{21} & p_{22} \end{bmatrix} = \begin{bmatrix} \cos \gamma & \sin \gamma \\ -\sin \gamma & \cos \gamma \end{bmatrix}. \quad (20)$$

The backscattering matrix including polarization rotation effect,  $S^p$ , is given by

$$\begin{aligned} S^p &= P(-\gamma) T P(\gamma) P(-\gamma) S^b P(\gamma) P(-\gamma) T P(\gamma) \\ &= P(-\gamma) T S^b T P(\gamma) \\ &= P(-\gamma) S' P(\gamma). \end{aligned} \quad (21)$$

If it is noted that  $p_{11} = p_{22}$  and  $p_{12} = -p_{21}$ , then the biased backscattering matrix for the PTWR is given by

$$\begin{aligned} S^p &= \begin{bmatrix} s_{11}^p & s_{12}^p \\ s_{21}^p & s_{22}^p \end{bmatrix} \\ s_{11}^p &= p_{11}^2 s_{hh}' + p_{21}^2 s_{vv}' + 2p_{11}p_{21}s_{hv}' \\ s_{12}^p &= p_{11}p_{21}(s_{vv}' - s_{hh}') + (p_{11}^2 - p_{21}^2)s_{hv}' \\ s_{21}^p &= p_{11}p_{21}(s_{vv}' - s_{hh}') + (p_{11}^2 - p_{21}^2)s_{hv}' \\ s_{22}^p &= p_{21}^2 s_{hh}' + p_{11}^2 s_{vv}' - 2p_{11}p_{21}s_{hv}'. \end{aligned} \quad (22)$$

For most meteorological observations, hydrometeors are assumed to have a vertical axis of symmetry, and therefore  $s_{hv}^{(b)} = s_{vh}^{(b)} = 0$  [21]. Thus, (22) can be simplified to

$$S^p = P^T(\gamma) S' P(\gamma) = \begin{bmatrix} p_{11}^2 s_{hh}' + p_{21}^2 s_{vv}' & p_{11}p_{21}(s_{vv}' - s_{hh}') \\ p_{11}p_{21}(s_{vv}' - s_{hh}') & p_{21}^2 s_{hh}' + p_{11}^2 s_{vv}' \end{bmatrix}. \quad (23)$$

Theoretically, the unbiased backstattering matrix  $S'$  can be recovered by a simple multiplication with the inverse of rotation matrix as

$$S' = (P^T(\gamma))^{-1} S^{(p)} P^{-1}(\gamma) = C^T S^{(p)} C \quad (24)$$

where the correction matrix  $C$  is defined as

$$C = P^{-1}(\gamma) = \begin{bmatrix} \cos \gamma & -\sin \gamma \\ \sin \gamma & \cos \gamma \end{bmatrix}. \quad (25)$$

However, the biased backscattering matrix  $S^p$  defined in (23) cannot be simultaneously measured by the PTWR. In general, four pulses separated by pulse repetition time  $T_s$  are required to establish  $S^p$ . The phase shifts caused by the scatterers' motion are different in consecutive measurements. Hence, the backscattering matrix has to be adjusted for the Doppler effect

before polarization correction can be applied [11]. Additionally, so far only the effect of the fields' misprojection has been considered. The antenna pattern is beam and polarization dependent and is characterized during initial system calibration, resulting in a set of calibration factors [ $C_{hh}(\phi')$ ,  $C_{hv}(\phi')$ ,  $C_{vh}(\phi')$ , and  $C_{vv}(\phi')$ ]. If both effects are included, then the biased backscattering matrix  $S^P$  can be defined as

$$\begin{aligned} S^{(P)} &= \begin{bmatrix} C_{hh}s_{hh}^{(P)}(2i) & C_{hv}s_{hv}^{(P)}(2i+3) \\ C_{vh}s_{vh}^{(P)}(2i+2) & C_{vv}s_{vv}^{(P)}(2i+1) \end{bmatrix} \\ &= \begin{bmatrix} C_{hh}s_{hh}^{(P)}(2i) & C_{hv}e^{-j2k_0 v3T_s} s_{hv}^{(P)}(2i) \\ C_{vh}e^{-j2k_0 v2T_s} s_{vh}^{(P)}(2i) & C_{vv}e^{-j2k_0 v1T_s} s_{vv}^{(P)}(2i) \end{bmatrix} \end{aligned} \quad (26)$$

where  $v$  is the radial velocity, and the arguments  $2i$ ,  $2i+1$ ,  $2i+2$ , and  $2i+3$  denote radar pulse indices.

Finally, under the assumption that  $s_{hv}^{(b)} = s_{vh}^{(b)} = 0$ , only the diagonal terms of the backscattering matrix are necessary in order to compute the unbiased standard weather radar products. First, the Doppler effect correction and the antenna pattern calibration factor should be implemented. Then, the unbiased elements of the backscattering matrix ( $s'_{hh}$ ,  $s'_{vv}$ ) can be simply obtained as follows:

$$\begin{aligned} s'_{hh} &= \frac{s_{vv}^{(P)} - \left(\frac{p_{11}}{p_{21}}\right)^2 s_{hh}^{(P)}}{p_{21}^2 - \frac{p_{11}^4}{p_{21}^2}} \\ s'_{vv} &= \frac{s_{vv}^{(P)} - \left(\frac{p_{21}}{p_{11}}\right)^2 s_{hh}^{(P)}}{p_{11}^2 - \frac{p_{21}^4}{p_{11}^2}}. \end{aligned} \quad (27)$$

The difference in antenna gain between co-polar channels is addressed during the initial system calibration.

#### ACKNOWLEDGMENT

The authors thank Prof. Saibun Tjuatja and Ms. S. Ermis of the Electrical and Computer Engineering Department and Prof. D. J. Seo of the Civil Engineering Department of the University of Texas at Arlington for their logistical support. Prof. J. Salazar and Dr. R. Medina are acknowledged for their significant contributions to the development of the PTWR. The authors also thank Mr. E. Lyons for providing CASA XUTA radar data.

#### REFERENCES

- [1] D. S. Zrnić *et al.*, "Agile-beam phased array radar for weather observations," *Bull. Amer. Meteor. Soc.*, vol. 88, pp. 1753–1766, Nov. 2007.
- [2] P. L. Heinselman, D. L. Priegnitz, K. L. Manross, T. M. Smith, and R. W. Adams, "Rapid sampling of severe storms by the national weather radar testbed phased array radar," *Weather Forecasting*, vol. 23, no. 5, pp. 808–824, 2008.
- [3] J. Wurman and M. Randall, "An inexpensive, mobile, rapid-scan radar," in *Proc. 30th Int. Conf. Radar Meteorol.*, Munich, Germany, 2001, p. P3.4.
- [4] H. B. Bluestein, M. M. French, I. Popstefanija, R. T. Bluth, and J. B. Knorr, "A mobile, phased-array Doppler radar for the study of severe convective storms: The MWR-05XP," *Bull. Amer. Meteor. Soc.*, vol. 91, no. 5, pp. 579–600, 2010.
- [5] B. Isom *et al.*, "The atmospheric imaging radar (AIR) for high-resolution observations of severe weather," in *Proc. IEEE Radar Conf.*, Kansas City, MO, USA, May 2011, pp. 627–632.
- [6] J. L. Salazar, R. Medina, E. J. Knapp, and D. J. McLaughlin, "Phase-tilt array antenna design for dense distributed radar networks for weather sensing," in *Proc. Int. Geosci. Remote Sens. Symp.*, Boston, MA, USA, Jul. 2008, pp. V-318–V-321.
- [7] A. P. Hopf *et al.*, "CASA Phased Array Radar System description, simulation and products," in *Proc. Int. Geosci. Remote Sens. Symp. (IGARSS)*, Cape Town, South Africa, Jul. 2009, pp. II-968–II-971.
- [8] K. Orzel *et al.*, "Mobile X-band dual polarization phased array radar: System requirements and development," in *Proc. 35th Conf. Radar Meteorol.*, Pittsburgh, PA, USA, Sep. 2011, p. 14A.4.
- [9] H. B. Bluestein *et al.*, "Radar in atmospheric sciences and related research: Current systems, emerging technology, and future needs," *Bull. Amer. Meteor. Soc.*, vol. 95, no. 12, pp. 1850–1861, 2014.
- [10] G. Zhang, R. J. Doviak, D. S. Zrnić, J. Crain, D. Staiman, and Y. Al-Rashid, "Phased array radar polarimetry for weather sensing: A theoretical formulation for bias corrections," *IEEE Trans. Geosci. Remote Sens.*, vol. 47, no. 11, pp. 3679–3689, Nov. 2009.
- [11] D. S. Zrnić, G. Zhang, and R. J. Doviak, "Bias correction and Doppler measurement for polarimetric phased-array radar," *IEEE Trans. Geosci. Remote Sens.*, vol. 49, no. 2, pp. 843–853, Feb. 2011.
- [12] K. Orzel, V. Venkatesh, T. Hartley, and S. Frasier, "Development of a X-band dual polarization phased array radar," in *Proc. IEEE Radar Conf. (RadarCon)*, Ottawa, ON, Canada, Apr./May 2013, pp. 1–4.
- [13] V. Chandrasekar *et al.*, "The CASA Dallas Fort Worth remote sensing network ICT for urban disaster mitigation," in *Proc. EGU General Assembly Conf. Abstracts*, 2013.
- [14] A. Bajaj and B. Philips, "Casting the net a revolutionary business model for deploying weather radar networks," in *Meteorological Technology International*. Dorking, U.K.: UKIP Media & Events, Ltd., Aug. 2012, pp. 106–108.
- [15] H. Chen and V. Chandrasekar, "The quantitative precipitation estimation system for Dallas–Fort Worth (DFW) urban remote sensing network," *J. Hydrol.*, vol. 531, pp. 259–271, Dec. 2015.
- [16] M. Sachidananda and D. S. Zrnić, "Efficient processing of alternately polarized radar signals," *J. Atmos. Ocean. Technol.*, vol. 6, no. 1, pp. 173–181, Feb. 1989.
- [17] T. ChandraSekar, "Dual polarized staggered PRT scheme for weather radars: Analysis and applications," *IEEE Trans. Geosci. Remote Sens.*, vol. 33, no. 2, pp. 239–246, Mar. 1995.
- [18] E. J. Knapp, J. Salazar, R. H. Medina, A. Krishnamurthy, and R. Tessier, "Phase-tilt radar antenna array," in *Proc. 41st Eur. Microw. Conf. (EuMC)*, Oct. 2011, pp. 1055–1058.
- [19] Y. Wang and V. Chandrasekar, "Polarization isolation requirements for linear dual-polarization weather Radar in simultaneous transmission mode of operation," *IEEE Trans. Geosci. Remote Sens.*, vol. 44, no. 8, pp. 2019–2028, Aug. 2006.
- [20] R. H. Medina, E. J. Knapp, J. L. Salazar, and D. J. McLaughlin, "T/R module for CASA phase-tilt radar antenna array," in *Proc. 42nd Eur. Microw. Conf. (EuMC)*, Oct. 2012, pp. 1293–1296.
- [21] L. Lei, G. Zhang, and R. J. Doviak, "Bias correction for polarimetric phased-array radar with idealized aperture and patch antenna elements," *IEEE Trans. Geosci. Remote Sens.*, vol. 51, no. 1, pp. 473–486, Jan. 2013.
- [22] H. Liu and V. Chandrasekar, "Classification of hydrometeors based on polarimetric radar measurements: Development of fuzzy logic and neuro-fuzzy systems, and *in situ* verification," *J. Atmos. Ocean. Technol.*, vol. 17, no. 2, pp. 140–164, Feb. 2000.
- [23] F. Junyent, V. Chandrasekar, D. McLaughlin, E. Insanic, and N. Bharadwaj, "The CASA integrated project 1 networked radar system," *J. Atmos. Ocean. Technol.*, vol. 27, no. 1, pp. 61–78, 2010.
- [24] M. Zink, E. Lyons, D. Westbrook, J. Kurose, and D. L. Pepyne, "Closed-loop architecture for distributed collaborative adaptive sensing of the atmosphere: Meteorological command and control," *Int. J. Sensor Netw.*, vol. 7, nos. 1–2, pp. 4–18, Jan. 2010.
- [25] A. V. Ryzhkov and D. S. Zrnić, "Depolarization in ice crystals and its effect on radar polarimetric measurements," *J. Atmos. Ocean. Technol.*, vol. 24, no. 7, pp. 1256–1267, Jul. 2007.
- [26] A. V. Ryzhkov, "Interpretation of polarimetric radar covariance matrix for meteorological scatterers: Theoretical analysis," *J. Atmos. Ocean. Technol.*, vol. 18, no. 3, pp. 315–328, Mar. 2001.
- [27] D. Zrnić, R. Doviak, G. Zhang, and A. Ryzhkov, "Bias in differential reflectivity due to cross coupling through the radiation patterns of polarimetric weather radars," *J. Atmos. Ocean. Technol.*, vol. 27, no. 10, pp. 1624–1637, Oct. 2010.
- [28] R. J. Doviak and D. S. Zrnić, *Doppler Radar and Weather Observations*. New York, NY, USA: Dover, 1993.



**Krzysztof A. Orzel** received the Dipl.-Ing. degree in electrical engineering from the Karlsruhe Institute of Technology, Karlsruhe, Germany, in 2008, and the Ph.D. degree in electrical and computer engineering from the University of Massachusetts Amherst, Amherst, MA, USA, in 2015.

From 2007 to 2008, he was with the German Aerospace Center, Cologne, Germany, contributing to the development of a full body scanner for aviation safety and homeland security. In 2009, he joined the Microwave Remote Sensing Laboratory, University of Massachusetts Amherst, as a Research Assistant, where he first had an opportunity to participate in a multiagency field project to study tornadoes (VORTEX2). His current research interests include radar systems design, signal processing, and radar-based UAV detection and classification.



**Stephen J. Frasier** received the B.E.E. degree from the University of Delaware, Newark, DE, USA, in 1987, and the Ph.D. degree from the University of Massachusetts Amherst, Amherst, MA, USA, in 1994.

From 1987 to 1990, he was with SciTec, Inc., Princeton, NJ, USA. In 1990, he joined the Microwave Remote Sensing Laboratory, University of Massachusetts, first as a Research Assistant and subsequently as a Research Fellow. In 2012, he spent a sabbatical with Météo-France, Toulouse, France, performing research with an X-band weather radar network deployed in the maritime Alps. In 1997, he joined the faculty at the University of Massachusetts, where he is currently a Professor and the Co-Director of the Microwave Remote Sensing Laboratory. His current research interests include microwave imaging and interferometry, phased-array radar, radar oceanography, and radar meteorology.

Dr. Frasier is a Senior Member of the IEEE Geoscience and Remote Sensing Society and a member of URSI Commission F, the American Geophysical Union, and the American Meteorological Society.